Available online at www.sciencedirect.com
SCIENCE DIRECT®
Journal of Nuclear Materials 323 (2003) 290–303
journal of nuclear materials
www.elsevier.com/locate/jnucmat

On dislocation–defect interactions and patterning: stochastic discrete dislocation dynamics (SDD)

M. Hiratani [a], H.M. Zbib [b,*]

[a] Chemistry and Material Science Directorate, Lawrence Livermore National Laboratory, CA 94551, USA
[b] School of Mechanical and Materials Engineering, Washington State University, Pullman, WA 99164-2920, USA

Abstract

The problem of dislocation patterning and interaction of threading dislocations with immobile dislocation loops and defects is investigated analytically and computationally based on a statistical analysis and a recently developed model of discrete stochastic dislocation dynamics (SDD), respectively. The statistical analysis is based on the Friedel–Kocks model and shows the validity of the Friedel relation for the critical resolved stress while a power law with different stress dependence is obtained for the average pinning distance on a stable dislocation array. The difference of the stress dependence is attributed to each model assumptions, such as stable dislocation configurations in athermal system or meta-stable configurations in thermally activated system. The SDD computational study includes thermal and strain fluctuation, predicting non-trivial fractal instability of the plastic strain. The height difference correlations of the plastic strain show that the external load causes a multifractality, and enhances the instability at higher order moments.

PACS: 03.20.+i; 03.40.−t; 05.20.−y

1. Introduction

Configurations of dislocations including entanglements or networks may be classified as loops, non-loops (threading dislocation), or combinations of them. Many of the inherent localized obstacles, such as the Frank-sessile loops or stacking fault tetrahedra, are small dislocation loops with short-range stress field, typically in a form of $\sigma \propto r^{-m}$ with $m \geqslant 3$, while a threading dislocation has a long-range field with $1 \leqslant m < 3$. Accordingly, the dislocation self-energy E, or the effective mass density of a dislocation loop is finite even though the size of material is infinite. However, the self-energy of a threading dislocation is infinite and has a logarithmic form, i.e., $E \propto \ln(R/\vec{r}_0)$ where R is some upper bound of what, and $E \to \infty$ as $R \to \infty$ and $\vec{r}_0$ is the dislocation core radius. The qualitative difference between these two forms of dislocations reflects changes in material geometry. If the threading dislocations have a non-zero net Burgers vector through a region of interest then these dislocations cause material deformation (bending and/or twisting). Such dislocations are referred to as geometrically necessary dislocations (GNDs). However, dislocation loops that are contained within the same region involve no shape change (on average) and are referred to as statistically stored dislocations (SSDs). Although the net shape of the material remains the same regardless of the density of the SSDs, the SSDs affect the plastic behavior through their interaction with the GNDs.

Dislocations also interact with other types of point defects and defect clusters. Due to the low activation energy, vacancies or interstitials are easily formed by thermal fluctuations. Other sources of energy such as high-energy beams can also induce increments of population of point obstacles. Moreover, defect clusters such as micro-voids, precipitates, or small prismatic dislocation loops can be formed by migration and condensation of point defects. Although some types of self-interstitial atoms clusters (SIAs) or dislocation loops can

* Corresponding author. Tel.: +1-509 335 7832; fax: +1-509 335 4662.
E-mail address: zbib@wsu.edu (H.M. Zbib).

0022-3115/$ - see front matter
doi:10.1016/j.jnucmat.2003.08.042

migrate by thermal activation, many of these defects are sessile or nearly sessile and act as local barriers against glissile dislocations. It is believed that these defects are responsible for the micro-yield in the initial stage of deformation since glissile dislocations are more likely to encounter these defects than forest dislocations.

Other important types of defect clusters are stacking fault tetrahedra (SFTs) and Frank sessile loops (FSLs). These types of defects can be modeled as immobile dislocation loops and are commonly found in FCC metals with low stacking fault energy. Perfect dislocation loops (as opposed to FSLs) also form in materials with high stacking fault energy. In some irradiated BCC metals, both mobile perfect edge loops and sessile loops are observed. As shown in the following sections, various precipitates in alloys can also be represented as combination of dislocation loops and thus can be treated within the same framework. In this work, the interaction between small dislocation loops/defects and threading dislocations is investigated, focusing mainly on micro-yield or easy glide in the initial deformation stage. In the next section, the critical resolved shear stress (CRSS) τ_c in athermal glide is derived and Friedel relations are reconsidered. In Section 3, the effects of thermal fluctuation on dislocation motion among sessile dislocation loops and its peculiar behavior are described. In Section 4 we discuss the result of this work and its implication to continuum models with higher order strain gradients.

2. Statistical properties of dislocation segment arrays

Considerable research has been devoted to determine the CRSS for dislocations interacting with localized obstacles, corresponding to different types of defects. For example, in irradiated copper high defect cluster density of the order of $\sim 10^{22}/\mathrm{m}^3$ the average spacing L_0 between the clusters is about 45 nm and the average cluster size r_0 a few nm (in many cases $r_0 \ll L_0$). In a simplified model [1] for easy glide, identical point-like obstacles with strength F_c are randomly distributed on a glide plane, and a glissile dislocation with constant line tension Γ interacts with the pinning obstacles. Under a resolved shear stress, the mechanical stability of a bowing dislocation–obstacle configuration is maintained until the dislocation force $2\Gamma\sin(\theta/2)$ exceeds a critical force F_c $(= 2\Gamma\sin(\theta_c/2))$ (see Fig. 1 for the angle of attack θ). The expression for the CRSS is given by the so-called Friedel relation [1] as

$$\tau_c = \alpha(F_c/2\Gamma)^{3/2}\tau_o \tag{1a}$$

and the average dislocation segment length between the neighboring pinning obstacles is given as

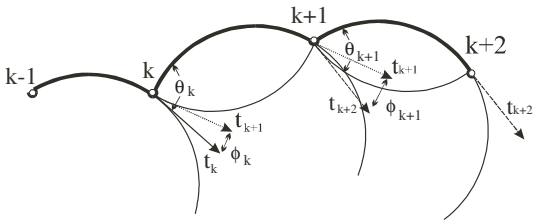

Fig. 1. Dislocation–obstacle array properties. θ, ϕ, t denote the angle of attack, angle of deviation, and line senses at each obstacle site, respectively.

$$\langle l_0\rangle = \alpha' L_0(\tau_o/\tau)^{1/3} \quad (\tau \leqslant \tau_c), \tag{1b}$$

where α and α' are numerical constants of order of unity, and τ_o is the Orowan stress defined here with the magnitude of Burgers vector b as $\tau_o \equiv 2\Gamma/bL_0$. Therefore, a dispersion hardening law follows $\tau_c \propto L_0^{-1}$ which is different from other obstacle related flow rules such as the Taylor–Mott type forest hardening law $\tau_c \propto L_d^{-1/2}$ or the Hall–Petch relation for polycrystalline materials $\tau_c \propto L_g^{-1/2}$, where L_d and L_g are the average dislocation spacing and grain size, respectively. Eq. (1) is derived for a simple equidistant two-segment configuration, which is used as a typical dislocation–obstacle configuration. The same functional forms have also been derived by other researchers using statistical approaches [2–6]. Although some computational analyses [7] confirmed Eq. (1b) at finite temperatures, a different power law has been found at zero temperature in the present study. Next we derive the statistical properties of dislocation–obstacle arrays.

2.1. Derivation of the CRSS for the same kind of localized sessile loops

We follow the notations and assumptions made by Hanson and Morris [2,3] and Labusch [5] for dislocation segment arrays that form on a glide plane. For simplicity, we normalize the segment length l (between successive obstacles), stress σ, and dislocation force f by 2Γ, τ_o, and L_0, respectively, and re-write Eqs. (1) as

$$\sigma_c = f_c^{3/2}, \tag{2a}$$

$$\langle l\rangle = \sigma^{-1/3} \quad (\sigma \leqslant \sigma_c). \tag{2b}$$

With this normalization, obstacles are now distributed randomly with average concentration of unity, and hence, the glide area element dA represents the probability of finding dA obstacles. Stable dislocation segment arrays are constructed by the circle-rolling method: the circle with dimensionless radius of curvature R $(= 1/2\sigma)$ is rotated around each obstacle at $\theta \leqslant \theta_c$ until the next obstacle is found, otherwise the search process is repeated starting from the previous obstacle. The search

process continues until the array of designated size is constructed. One of the quantity to characterize the constructed segment array is the deviation angle ϕ or total deviation angle ψ $(=\sum_i \phi_i)$. When the mean value $\langle\phi\rangle$ is not zero, the search process should stop after the segment arrays form loops of size of $\sim|\pi/\langle\phi\rangle|$ while it remains macroscopically straight without the need for termination of array construction.

By inspecting the geometry associated with the search algorithm, the area element is expressed as $\mathrm{d}A = l\,\mathrm{d}l\,\mathrm{d}\phi$, and the distribution function $g_0(\phi)$ within the search area as

$$g_0(\phi)\,\mathrm{d}\phi = \left(\int l\,\mathrm{d}l\right)\mathrm{d}\phi \quad \text{is}$$

$$\begin{aligned} g_0(\phi)\,\mathrm{d}\phi \equiv 2R^2 \cdot \{&\sin^2[(\theta_c-\phi)/2][u(\phi)-u(\phi-\theta_c)] \\ &+ \{\sin^2[(\theta_c-\phi)/2] - \sin^2(\phi/2)\} \\ &\cdot [u(\phi-\theta_c+\pi)-u(\phi)] + \cos^2(\phi/2) \\ &\times [u(\phi+\pi)-u(\phi-\theta_c+\pi)]\}\,\mathrm{d}\phi, \end{aligned} \tag{3}$$

where $u(x)$ is the step function i.e. $u(x \geqslant 0) = 1$ and $u(x<0)=0$. For connection of the kth segment between the kth and $k+1$th obstacles, the probability $p_{(k)}$ of finding $k+1$th obstacle at a position is given as

$$p_{(k)} = g_0(\phi_k)\delta\phi = g_0(\psi_{(k+1)} - \psi_{(k)})\delta\psi. \tag{4a}$$

To assign the probability of a position of the kth obstacle within the search area, the area is divided into M area elements. Then the probability for kth obstacle in the mth area element $(m = 1,2,\ldots,M)$ is $p_{(k)} = g_0(\phi_{(k)m})\delta\phi$ where $\phi_{(k)m} = -\pi + (m/M)(\pi+\theta_c)$. Since there are M possible positions for each connection, there are kM possible positions for the total deviation angle $\psi_{(k)}$ for kth obstacle (after k segment connections). Indexing the corresponding position for $\psi_{(k)}$ with n $(n = 1,2,\ldots,kM)$, the probability in Eq. (4a) is given in terms of new indices as m and n

$$p_m = g_0(\phi_{(k)m})\delta\phi = g_0(\psi_{(k+1)n+m} - \psi_{(k)n})\delta\psi, \tag{4b}$$

where $\psi_{(k)n} = -k\pi + (n/M)(\pi+\theta_c)$. This p_m gives a transitional probability, which depends on the initial position of the kth obstacle and the final position of the $k+1$th obstacle. Similarly, the total transition probability for the Nth segment arrays depends on the difference of the positional indices for the first obstacle and the Nth obstacle. When the difference of the indices is q, it is expressed as [8]

$$p(N,q) = T^N_{q+1,1}, \tag{5a}$$

where T is a $NM \times NM$ cyclic matrix given as

$$T = \begin{pmatrix} p_0 & 0 & \cdots & \cdots & \cdots & \cdots & 0 & p_{M-1} & \cdots & p_2 & p_1 \\ p_1 & p_0 & 0 & \ddots & \ddots & \ddots & \ddots & 0 & \ddots & \ddots & p_2 \\ \vdots & p_1 & p_0 & \ddots & \ddots & \ddots & \ddots & \ddots & \ddots & \ddots & \vdots \\ p_{M-1} & \vdots & p_1 & \ddots & \ddots & \ddots & \ddots & \ddots & \ddots & 0 & p_{M-1} \\ 0 & p_{M-1} & \vdots & \ddots & \ddots & \ddots & 0 & \ddots & \ddots & \ddots & 0 \\ \vdots & 0 & p_{M-1} & \ddots & \ddots & \ddots & \ddots & \ddots & \ddots & \ddots & \vdots \\ \vdots & \ddots & 0 & \ddots & \ddots & \ddots & \ddots & \ddots & \ddots & \ddots & \vdots \\ \vdots & \ddots & \ddots & \ddots & \ddots & \ddots & \ddots & \ddots & \ddots & \ddots & \vdots \\ \vdots & \ddots & 0 & \ddots & 0 & p_{M-1} & \cdots & p_1 & p_0 & 0 & \vdots \\ \vdots & \ddots & \ddots & \ddots & \ddots & 0 & p_{M-1} & \cdots & p_1 & p_0 & 0 \\ 0 & \cdots & \cdots & \cdots & \cdots & \cdots & 0 & P_{M-1} & \cdots & p_1 & p_0 \end{pmatrix}.$$

By determining the eigenvalues of T as shown in Appendix A, Eq. (5a) is rewritten in terms of p_m as

$$p(N,q) = \sum_{n=0}^{NM-1} f(\mathrm{e}^{2in/NM})^N \mathrm{e}^{-2inq/NM}/NM, \tag{5b}$$

where $f(x) = \sum_{m=0}^{M-1} p_m x^m$.

Replacing the summation in Eq. (5b) with integration in the limit of large M, and discrete variable ψ_n (or ϕ_m) for continuous $\psi(\phi)$, we obtain P for arbitrary (finite) array size N as

$$\begin{aligned} P(N,\psi) = -\mathrm{i}R^{2N} \sum_{p,q=0}^{(N-1)/2} &(-1)^{(N-1)/2+p}\,{}_N\mathrm{C}_p\,{}_N\mathrm{C}_q \\ &\cdot \{\Lambda[\psi - (N-p)\theta_c + q\pi] \\ &- \Lambda[\psi - p\theta_c + (N-q)\pi] \\ &+ \Lambda[\psi - (N-p)\theta_c + (N-q)\pi] \\ &- \Lambda[\psi - p\theta_c + q\pi]\} \end{aligned} \tag{6a}$$

for odd N, and

$$\begin{aligned} P(N,\psi) = R^{2N} \sum_{p,q=0}^{N/2-1} &(-1)^{N/2+p}\,{}_N\mathrm{C}_p\,{}_N\mathrm{C}_q \\ &\cdot \{\Lambda[\psi - (N-p)\theta_c + q\pi] \\ &+ \Lambda[\psi - p\theta_c + (N-q)\pi] \\ &+ \Lambda[\psi - (N-p)\theta_c + (N-q)\pi] \\ &+ \Lambda[\psi - p\theta_c + q\pi]\} + {}_N\mathrm{C}_{N/2N}\mathrm{C}_p(-1)^{N/2+p} \\ &\times \left\{\Lambda\left[\psi - (N-p)\theta_c + N\frac{\pi}{2}\right]\right. \\ &\quad \left. + \Lambda\left[\psi - p\theta_c + N\frac{\pi}{2}\right]\right\} \\ &+ {}_N\mathrm{C}_{N/2N}\mathrm{C}_q\left\{\Lambda\left[\psi - N\frac{\theta_c}{2} + q\pi\right]\right. \\ &\quad \left. + \Lambda\left[\psi - N\frac{\theta_c}{2} + (N-q)\pi\right]\right\} \\ &+ ({}_N\mathrm{C}_{N/2})^2\Lambda\left(\psi - N\frac{\theta_c - \pi}{2}\right) \end{aligned} \tag{6b}$$

Table 1
The dependence of size and obstacle strength on the ratio σ_{cN}/σ_c

N	$\theta_c = 0.005$	$\theta_c = 0.01$	$\theta_c = 0.02$	$\theta_c = 0.05$	$\theta_c = 0.1$	$\theta_c = 0.2$	$\theta_c = 0.4$	$\theta_c = 0.8$
1	11.9224	8.4304	5.9611	3.7698	2.6648	1.8820	1.3241	0.9176
5	1.5158	1.4142	1.3195	1.2038	1.1227	1.0458	0.9690	0.8792
11	1.1867	1.1499	1.1142	1.0686	1.0350	1.0011	0.9630	0.9060
21	1.0854	1.0677	1.0502	1.0274	1.0101	0.9917	0.9683	0.9240
51	1.0172	1.0129	1.0085	1.0027	0.9980	0.9919	0.9802	0.9463
101	1.0097	1.0070	1.0043	1.0007	0.9976	0.9931	0.9830	0.9504
201	1.0049	1.0034	1.0018	0.9997	0.9977	0.9944	0.9854	0.9538

for even N where

$$\Lambda(\psi) = \mathrm{sgn}(\psi)\cdot[2\mathrm{i}^N\Gamma(3N)]^{-1}\psi^{3N-1} \times {}_1F_2\left(N;\frac{3N}{2}+\frac{1}{2},\frac{3N}{2},\frac{-\psi^2}{4}\right).^1$$

When the mean deviation angle is not zero $\langle\phi\rangle = \psi/N \neq 0$, loops are formed and Eq. (6) is valid up to $N \sim |\pi/\langle\phi\rangle$ otherwise $P(N,\psi) = 0$. For (macroscopically) straight dislocation arrays, Eq. (6) can be simplified as

$$P(N,0) = 2\mathrm{i}R^{2N}\sum_{p=0}^{N}\sum_{q=0}^{[p\theta_c/\pi]}\sum_{q=0}(-1)^{(N-1)/2+p}{}_NC_{PN}C_q\Lambda[-p\theta_c+q\pi] \tag{7a}$$

for odd N, and

$$P(N,0) = 2R^{2N}\sum_{p=0}^{N/2}\sum_{q=0}^{[(N-p)\theta_c/\pi]}(-1)^{N/2+p}{}_NC_P{}^NC_q\Lambda[-(N-p)\theta_c+q\pi] \tag{7b}$$

for even N. Furthermore, for (infinitely) large straight dislocation arrays, P is obtained using the method of the steepest descent for evaluating Eq. (5b) as [5]

$$P_L(N,0) = Z^N, \tag{8a}$$

where Z denotes the individual partition function, and it is given for weak obstacles as

$$Z = \int_A \mathrm{e}^{-y_0^*\phi}\,\mathrm{d}A = \int_{-\pi}^{\theta_c}\mathrm{e}^{-y_0^*\phi}g(\phi)\,\mathrm{d}\phi = R^2\theta_c^3\times 0.7035, \tag{8b}$$

where y_0^* is a characteristic parameter that satisfies the straight condition

$$\langle\phi\rangle = \int_A \phi\mathrm{e}^{-y_0^*\phi}\,\mathrm{d}A \Big/ \int_A \mathrm{e}^{-y_0^*\phi}\,\mathrm{d}A = \partial_{-y_0^*}\ln Z = 0 \tag{8c}$$

and numerical solution gives $y_0^* = -2.821/\theta_c$. The CRSS can be obtained from the condition $P_{(L)}(N,0)^{1/N} = 1$ that demarcates the stable continuation of arrays $(P_{(L)}(N,0) \geqslant 1)$ from unstable as $(P_{(L)}(N,0) \to 0)$ as N increases. In the limit of weak obstacle strength $(\theta_c \to 0)$ and for straight dislocation, Eq. (8b) yields

$$\sigma_c = 1/2R = \theta_c^{3/2}\times 0.4194 \tag{9a}$$

or in real dimension

$$\tau_c = \tau_o\theta_c^{3/2}\times 0.4194. \tag{9b}$$

For general size (N) and obstacle strength (θ_c), the deviation of the CRSS from the value in Eq. (9a) can be obtained as the ratio of the probabilities as $\sigma_{cN}/\sigma_c = \sqrt{P_L(N,0)/P(N,0)}$. Several values of the ratio of the CRSS for cases of finite array size to the large array size are given in Table 1.

Corrections to the degeneracy problem and priority problem associated with the array construction history yields lower values for the CRSS. The first order correction to the degeneracy problem [5] results in

$$\tau_c^{d,1} = \tau_o\theta_c^{3/2}\times 0.3359 \tag{9c}$$

while the 1st and 20th order corrections to the priority problem [9] respectively generate

$$\tau_c^{p,1} = \tau_o\theta_c^{3/2}\times 0.3837, \tag{9d}$$

$$\tau_c^{p,20} = \tau_o\theta_c^{3/2}\times 0.3769. \tag{9e}$$

Comparing these values with Eq. (2a), the original Friedel's value with numerical factor of unity is just several percent off the most-likely value. The validity of the Friedel relation for the CRSS is, therefore, justified.

2.2. Derivation of the CRSS for different kinds of loops

In general cases, variations of the pinning strength may be affected by the distribution of loop size, distance from the glide plane, orientation, etc. In this subsection, the problem of the mechanical stability of the glissile threading dislocation is considered for cases of different kinds of sessile localized loops within the same model

[1] ${}_1F_2$ is a generalized hypergeometric series: ${}_1F_2(a;b,c,\psi) = \sum_{k=0}^{\infty}\{(a)_k/[(b)_k(c)_k]\}(\psi^k/k!)$.

assumptions. For cases of two different kinds of localized obstacles, various empirical rules are used. For instance, a superposition law $\tau_{\text{tot}}^p = \tau_1^p + \tau_2^p$ where $p = 1$ for linear addition, and $p = 2$ for Pythagorean addition rule [10], and the rules of mixture $\tau_{\text{tot}}^p = y_1^q \tau_1^p + y_2^q \tau_2^p$, where y_i is an obstacle concentration, and $p = 1$ and $q = 1/2$ [11] or $p = 1$ and $q = 1$ [12]. Utilizing the same procedure described above, the partition function and the CRSS are obtained in this study for the case of a macroscopically straight threading dislocation interacting with small sessile loops of different sizes. Following the same procedure described by Eqs. (8a)–(8c), the total transition probability for the M-segment dislocation is expressed as

$$P(M,0) = Z^M = (M!/M_1!M_2!) z_1^{M_1} z_2^{M_2} \tag{10a}$$

with the individual partition function without correction factor as

$$z_i(y^*) = -(N_i/N)R^2[\exp(-2f_i y^*) - 1]/y^{*3} \tag{10b}$$

and the straight condition as

$$\partial_{y^*}(1/M)\ln Z = \langle \phi \rangle = \psi/M = 0. \tag{10c}$$

Here the obstacles of total number of $N(= N_1 + N_2)$ are distributed on the glide plane with the area A while the stable threading dislocation is pinned by $M(= M_1 + M_2)$ obstacles, where N_1 and N_2 are the number of each type of defect. Accordingly, the length and stress are normalized by $L_0 = \sqrt{A/N}$ and $\tau_o = \mu b/L_0$, respectively. The obstacle numbers M_i are determined as function of N_i by optimizing the probability $P(M,0)$ with respect to M_i, i.e.,

$$\partial_{M_i} \ln P = 0. \tag{10d}$$

For the special case of weak obstacles with almost the same strength i.e. $|\Delta\theta/\bar{\theta} \ll 1$ where $\Delta\theta = \theta_{c2} - \theta_{c1}$ and $\bar{\theta} = (\theta_{c1} + \theta_{c2})/2$, by expanding the partition function and neglecting the terms of $O\lfloor(\Delta\theta/\bar{\theta})^2\rfloor$, we obtain the characteristic parameter, the obstacle concentration on the dislocation, and the CRSS respectively as

$$y^* = \bar{\theta} y_0^* (\theta_{c1} x_1 + \theta_{c2} x_2)/(\theta_{c1}^2 x_1 + \theta_{c2}^2 x_2), \tag{11a}$$

$$x_i \equiv M_i/M = y_i \theta_{ci}^3/(y_1\theta_{c1}^3 + y_2\theta_{c2}^3), \tag{11b}$$

$$\tau_c^2 = \tau_{c1}^2 + \tau_{c2}^2 \left(\sigma_c = \sqrt{y_1\sigma_{c1}^2 + y_2\sigma_{c2}^2} \right. \\ \left. \text{in dimensionless form} \right), \tag{11c}$$

where x_i and y_i stand for obstacle concentration on the pinned threading dislocation and the glide plane, y_0^* the characteristic parameter already defined above, and τ_{ci} the CRSS in cases of the identical obstacles as expressed in Eq. (9b). Hence, the Pythagorean-type hardening rule is derived for this mixing case.

Comparison with Eq. (11c) is made using the discrete dislocation dynamics (DD) [13–16] (DD is described in Section 3.2). All simulations are performed under the athermal creep condition for a pure edge dislocation in the single crystal iron. For different kinds of localized pinning loops, two cases are investigated: case 1: mixture of $\langle 1\,0\,0\rangle\{1\,0\,0\}$ square loops and $1/2\langle 1\,1\,1\rangle\{1\,1\,1\}$ hexagonal loops with the edge length of 10b, case 2: mixture of larger and smaller square loops with the length of 10b and 7.5b (see Fig. 2(a)). Such dislocation loops are observed in irradiated BCC metals [17]. In both cases, these loops are randomly arranged on the $(1\,\bar{1}\,0)$ glide plane with the average interval of 100b as illustrated in Fig. 2(a). Fig. 2(b) shows the DD simulation results for the CRSS. Analytical results using Eq. (11c) are also shown using the two simulation data with $y_1 = 1$ and $y_2 = 0$. It can be deduced from the figures that the hexagonal loops act as stronger obstacles than the square loops for

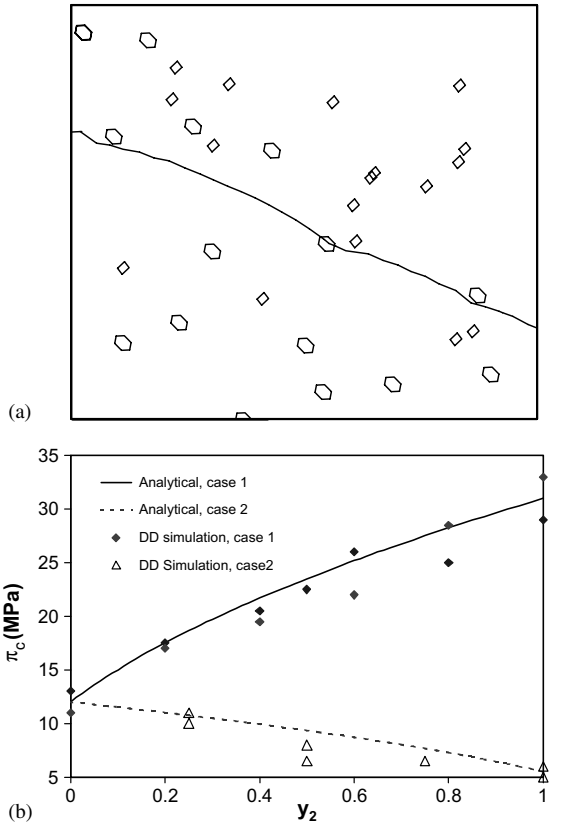

Fig. 2. (a) Snap shot of DD simulation for a threading dislocation interacting with hexagonal loops and square loops. (b) The CRSS for the mixing case as function of the concentration. y_2 stands for the relative concentration of the hexagonal loops (case 1) or smaller square loops (case 2).

case 1 while obviously larger square loops have stronger pinning force than the smaller ones in case 2. Although the scattering of the data indicates the difficulty of good samplings and precise determination of the CRSS by simulations, a strong correlation of data with Eq. (11c) is found in both cases.

2.3. Stress dependence of the average segment length

Analogous to the Eq. (8c) for the straight condition, the mean segment length without the aforementioned correction factors can be obtained as

$$\langle l\rangle = \int_A l\mathrm{e}^{-y^*\varphi}\,\mathrm{d}A \Big/ \int_A \mathrm{e}^{-y^*\varphi}\,\mathrm{d}A = R\theta_c \times 0.7089\cdots = \sigma^{-1}\theta_c = 0.3544\cdots \tag{12a}$$

Combining Eqs. (9a) with (12a) yields

$$\langle l\rangle = (\sigma_c^{2/3}/\sigma) \times 0.6326\cdots \tag{12b}$$

or in real dimension

$$\langle l_0\rangle = L_0(\tau_c^{2/3}\tau_o^{1/3}/\tau) \times 0.6326\cdots \tag{12c}$$

Hence, the mean segment length is inversely proportional to the resolved shear stress as compared with the original Friedel relation in Eq. (1b). $\langle l_0\rangle = \tau^{-1/3}$. The numerical constant is about 37% lower than the original value. When the correction to the priority problem is taken into consideration, we obtain different power laws $\langle l_0\rangle \propto \tau^{-m}$ where $m = 0.7281$ and 0.7218, with the 1st and 20th order corrections, respectively. Hence, stress dependence of the mean segment length is greater than the Friedel relation (since $\tau \ll \tau_o$), and its dependence coincides with each other only at the CRSS. This difference of the stress dependence arises from different model assumptions. The original Friedel relation in Eq. (2b) is derived for steady motion of dislocations among the dislocation forest by thermal activations [1]. This steady motion can be achieved under a strong geometrical condition that the activated dislocation segments encounter the next obstacle after sweeping one obstacle occupying area on average. Then the dislocation segment overcomes the next obstacle by thermal activation, and the process continues. On the other hand, Eq. (12c) is derived for the dislocation–obstacle configurations in athermal glide. Instead of the geometrical condition, they satisfy the maximum condition of the configurational entropy (or maximum probability), which denotes the most likely configuration. And hence, dislocation segments do not have to encounter the new obstacle nor dislocation motion is in steady manner even when the thermal activations are included.

In fact, the strong geometrical condition for the Friedel relation is satisfied only when the obstacle concentration is so high (or applied stress is so low) that every encountered obstacle is overcome by thermal activation, not by mechanical instability. In general, this is not always true since dislocations achieve a (meta-) stable configuration after some trial and error phenomenon (skipping obstacles). Near the CRSS, many obstacles are mechanically bypassed after one activation event [7]. Therefore, $\langle l_0\rangle$ in Eq. (2b) should be replaced by the distance between the sites of two successive active obstacles, rather than dislocation segment length between neighboring obstacles. Apparently Eq. (10c) should be applied to the dislocation segment length between neighboring obstacles in stable configuration.

Although the original Friedel relations or statistical relations derived above for weak obstacles are applicable to a wide range of physical problems, care must be taken for some cases. For instance, when the size of the effective stress field is comparable to the average obstacle spacing, which usually act as hard obstacles, the statistics are described by Mott–Orowan statistics. For large (strong) obstacles, equilibrium configurations are determined by force balance between forward and backward obstacle forces of finite depth. In addition, such hard obstacles contribute to the hardening through multiplication of the Orowan loops nucleated at each obstacle bypass. Furthermore, when kinks on dislocation are distinguishable such as those in screw dislocation in bcc structured metals or intermetallics, the dislocation–obstacle interaction is qualitatively different from that in the aforementioned string type dislocation. Coexistence of these two types of dislocation–obstacle interactions may provide a dislocation mechanism that generates peculiar plastic response [18].

3. Patterning in threading dislocation – loop interaction problems

3.1. General dislocation patterning

As shown above, dislocation statistics and mechanical stability of dislocations are largely controlled by the localized obstacles at the initial deformation stage. The problem of dislocation–obstacle interaction shows a close analogy with fluid percolation through porous media [19]. Based on the classification of the universality, Gil Sevillano et al. [19] described that the growth of threading dislocation shape near the CRSS follows either self-affine non-fractal patterns for weak obstacles such as those considered above, or self-similar fractal patterns for strong obstacles. The former case corresponds to Friedel statistics consistent with depinning transition for soft obstacles while the later to Mott–Orowan statistics consistent with conventional percolation transition for hard obstacles. The same problem was considered with conservative conditions for the angle θ and the segment length l before and after an

activation event [20]. In such a model the self-organized criticality (SOC) behavior is demonstrated for the spacing l between the activated obstacles, indicating that all length-scales are involved in the structural evolution.

Plastic deformation can be viewed as percolation events in which the behavior of plastic strain is characterized by the successive local bursts of dislocations [21]; repeatedly gaining and loosing temporal stable configurations. Accounting for the effect of shear bands, Thomson et al. [21] explained the SOC-type universal behavior of plastic strain and derived a scaling relation for the strain decay, i.e., $\langle \gamma(r+\Delta r)/\gamma(r)\rangle = r^{-\alpha} f(\Delta r/r_c)$ where Δr denotes distance from the spatial point where the strain initiates to point of interest, f is the scaling function, and r_c is he correlation length. Similar scaling relations are also observed experimentally in fractal dislocation cell patterns where misorientation angles' distribution can be well fitted by a single curve regardless of the loading conditions or type of materials [22].

The internal strain field of randomly distributed local obstacles generates stochastic perturbations to encountered dislocations, as compared with deterministic forces such as the applied load. This stochastic stress field also contributes to the spatial dislocation patterning in the later stages of deformation. Thus the strain field of local obstacles adds spatially irregular uncorrelated noise to the equation of dislocation motion [23]. Using a phenomenological Fokker–Plank equation for the dislocation dynamics, Zaiser [23] explained the emergence of homogeneous dislocation structures in the deterministic limit while inhomogeneous structures such as fractal dislocation cells in the stochastic limit.

3.2. Stochastic dislocation dynamics

In addition to the strain fields of random dislocations or local obstacles, thermal fluctuations also provide a source of stochasticity in dislocation dynamics. Some computational studies for the dislocation pinning-depinning transition by a kinetic Monte-Carlo model also reveal scaling relations for the dislocation velocity and the relaxation time at finite temperatures [24]. In the following, we report spatial–temporal patterning of threading dislocations under the influence of both random obstacle fields and thermal stresses.

Thermal fluctuations arise from dissipation mechanism due to collisions of dislocations with surrounding particles, such as phonons or electrons. Rapid collisions and momentum transfers result in random forces on dislocations. These stochastic collisions, in turn, can be regarded as time-independent noises of thermal forces acting on the dislocations. Suppose that the exertion of thermal forces follows a Gaussian distribution. Then, thermal fluctuations will most likely result in very small net forces due to mutual cancellations. However, they sometimes become large and may cause diffusive dislocation motion or thermal activation events such as overcoming obstacle barriers. In this study, results for dislocation motion and patterning are obtained by employing a simulation model that accounts not only for deterministic effects but also for stochastic forces; leading to a model we call 'discrete stochastic dislocation dynamics' (SDD).

Discrete dislocation dynamics (DD) have been developed and applied to various deformation problems during the past decade [13,14,25–27]. The DD method is an effective computational scheme that can address plasticity problems at the meso and nano scales. In the DD algorithm, dislocations are modeled as discontinuity lines in a continuum, which are then descreteized into small segments connected by nodes. The dynamics of these segments and nodes are determined based on equations of dislocation motion. In the algorithm developed by Zbib and co-workers, a linear approximation is used in which the driving forces are evaluated over the segment length using linear shape functions. The interactive forces between the segments are computed based on the linear theory of elasticity. In addition, drag forces due to dissipation, applied forces, image forces, and inertia effects, etc. are calculated, and the dislocation structure evolves based on a deterministic Newtonian equation of motion. Moreover, DD simulations involve dislocation core reactions using, sometimes, local rules for annihilations or formations of junctions or jogs. Within the framework of multiscale modeling, these local rules are established according to information extracted from atomistic simulations. The end result is a set of non-linear and coupled equations of motion for the nodes connecting the segments. (See a recent review article by Zbib and Diaz de la Rubia [28]).

Although the DD method has been extensively used by many researchers to investigate various plasticity problems, almost all current discrete dislocation dynamics models are essentially deterministic and based on athermal models. Hence, they cannot be employed to simulate thermal activation processes. For example, in the problems of dislocation–local obstacle interactions, such as the ones described in the previous section, the activation enthalpy of local obstacles can be low for weak obstacles and dislocations can intermittently migrate by thermal activation. However, in deterministic models such as DD, once the system forms a meta-stable configuration, say dislocations pinned by obstacles, it can be trapped in energetic local minima causing unphysical freeze. To avoid this unphysical trapping of dislocations, stochastic thermal agitations have been implemented into the equations of dislocation motion as random stress pulses [9]. In SDD model, the system includes externally applied forces due to stress $\boldsymbol{\sigma}^{A}$, Peach–Kohler forces among glissile dislocation segments on a glide plane ($\boldsymbol{\sigma}^{D}_{ij}$ between ith and jth segments) or defect segments $\boldsymbol{\sigma}^{S}_{i,j}$ (such as in SFTs between the ith segment

and kth SFT), drag force due to electrons (drag coefficient B_e) and phonons ($B_{\rm ph}$), and random forces ($\boldsymbol{\tau}$) are added in heuristic way to the equation of motion such that

$$\dot{\mathbf{r}}_i = \mathbf{v}_i, \quad i = 1, 2 \ldots, N,$$

$$m_1^* \dot{\mathbf{v}}_i = -\sum_{\text{electron,phonon}} B\mathbf{v}_i + \left(\sum_{j\neq 1} \boldsymbol{\sigma}_{i,j}^{\rm D} + \sum_k \boldsymbol{\sigma}_{i,k}^{\rm S} + \boldsymbol{\sigma}^{\rm A} + \boldsymbol{\tau} \right) \cdot \mathbf{b}_i \times \xi_i, \qquad (13)$$

where $\mathbf{r}_i$ is the position vector of the dislocation node i, $\mathbf{v}_i$ is its velocity vector, m^* is the effective mass density, N is the total number of nodes, $\sum B$ is the total drag coefficient, and ξ_i is the dislocation line sense. Then, based on the assumption of the Gaussian process, the thermal stress pulse has zero mean and no correlation [29,30] between the two difference times. This leads to the average peak height given as [9,31]

$$\tau_{\rm h} = \sqrt{2kT \sum B/(b^2 \Delta l \Delta t)}, \qquad (14)$$

where k denotes Boltzman constant, T absolute temperature of the system, b the magnitude of Burgers vector, Δt time step, and Δl is the dislocation segment length. Some values of the peak height are shown in Table 2 for typical combinations of parameters. Here, Δt is chosen to be 50 fs, roughly the inverse of the Debye frequency. Although Δl or Δt does not have a fixed value, such a restriction is imposed so that the system at the energetic global minima should reach thermal equilibrium. The validity of these parameters are checked by comparing the assigned system temperature (T) with the kinetic temperature of a dislocation with both ends fixed, which should coincide on average according to the equipartition law. We obtained $\Delta t <\sim 100$ fs, while the choice of Δl is so wide that it should be determined from the minimum scales of microstructures of interest. In this study, the size of the local obstacle is assumed to be in the order of nm and, therefore, Δl is also chosen to be in the same order. Typical combinations of parameters with Eq. (13) are shown in Table 2.

With the SDD method, one can treat cross-slip (a thermally activated process) in a more accurate manner, since the duration of waiting time and thermal agitations are naturally included in the stochastic process. Here, the SDD cross-slip model for fcc is based on the Escaig–Friedel (EF) mechanism where cross-slip of a screw dislocation segment may be initiated by an immediate dissociation and expansion of Shockley partials. This EF mechanism has been observed to have lower activation energy than the Shoeck–Seeger mechanism where the double super kinks are formed on the cross-slip plane. In the EF mechanism, the activation enthalpy ΔG depends on the interval of the Shockley partials (d) and the resolved shear stress on the initial glide plane (σ) (see the MD simulations of Rasmussen and Jacobsen [32] and Rao et al. [33]). The constriction interval L also depends on σ. The activation energy for cross-slip is computed using an empirical formula fitted to on the MD results of Rao et al. [33]. Fig. 3 depicts the $\Delta G(\sigma)$ for the case of copper where we chose the value of 1.2 eV for the activation free energy and 0.045 J/m^2 for stacking fault energy. This activation energy for stress assisted cross-slip is entered as an input data into the SDD code.

Within the SDD code, dislocations are represented as perfect dislocations while a pair of parallel Shockley partials are introduced in the case of screw dislocations only for stress calculation at forward ($+d/2$) and backward ($-d/2$) direction of the original perfect screw. Then a Monte-Carlo type procedure is used to select either the initial plane or the cross-slip plane according to the activation enthalpy. For simplicity, we set the regime of the barrier with area of $L \times d$ and strength of $\Delta G/Ld$. The virtual Shockley partials move according to the Langevin forces in addition to the systematic forces according to equation (13) until the partials overcome the barrier and the interval decreases to the core distance. The implementation of this model captures the anisotropic response of cross-slip activation process to

Table 2
The stress pulse peak height for various combinations of parameters, $\Delta t = 50$ fs

T (K)	$\sum B$ (μPa s)	$\tau_{\rm h}$ (MPa) ($\Delta l = 5b$)	$\tau_{\rm h}$ (MPa) ($\Delta l = 10b$)
0	2	11.5	8.11
50	5	40.6	28.7
100	10	81.1	57.4
300	30	256	181

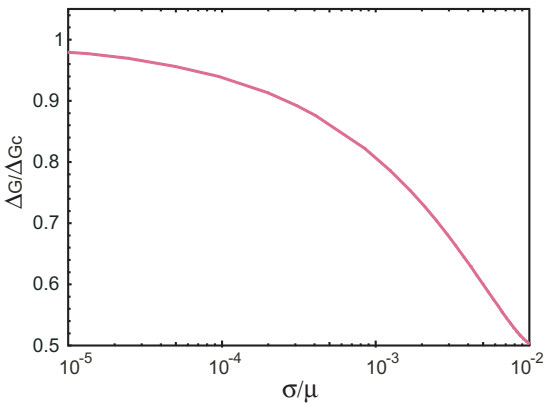

Fig. 3. The normalized activation enthalpy for copper as a function of the normalized resolved shear stress on the glide plane. $G_{\rm c}$ and μ denote the activation free energy and the shear modulus, respectively.

the loading direction, and consideration of the time duration (waiting time) during the cross-slip event, which have been missing in the former DD simulations (more details will be provided in a forthcoming article).

3.3. Multifractal behavior and patterning

The temporal–spatial behavior of threading dislocations is investigated in this study using the SDD model. A threading edge dislocation is placed among high density of SFTs with periodic boundary condition. The simulation is carried out with or without an applied external load. The total plastic strain tensor resulting from the motion of the dislocation segments and averaged over the computational cell is computed in the SDD model. Fig. 4(a) depicts the signal of plastic shear strains obtained by SDD simulation for the case with no applied external load. The fluctuations in the strain-time signal that can be seen in the figure can be attributed to both the strain field of the random SFTs and thermal

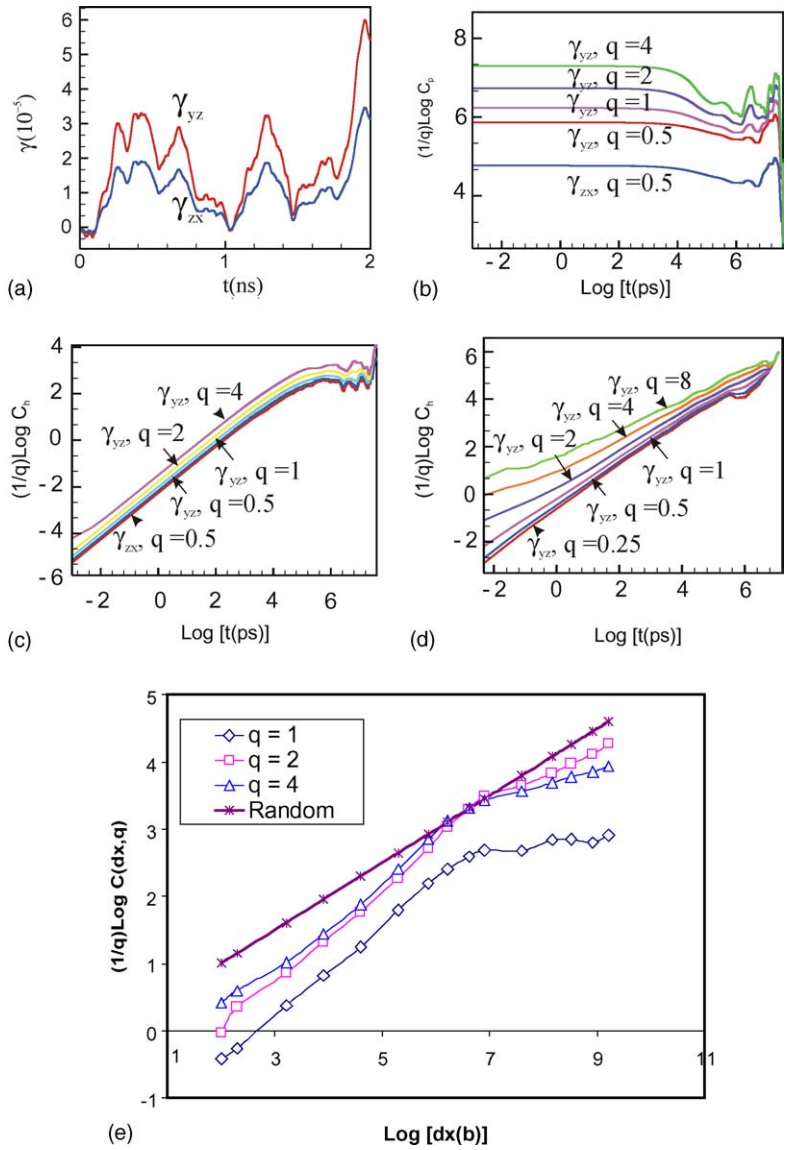

Fig. 4. (a) Plastic strain by single dislocation among stacking fault tetrahedron (SFTs) in copper. SFT density = $5.96\times10^{22}/m^3$, and no external stress is applied. (b) Pair correlation of two signals of plastic strain in Fig. 2(a). For clear view, one curve is shown for γ_{zx}. (c) Height correlation of two signals of plastic strain in Fig. 2(a). For clear view, one curve is shown for γ_{zx}. (d) Height difference correlation of two signals of plastic strain under 10 MPa of shear stresses. For clear view, only data for γ_{yz} is shown. (e) Height difference correlation for the threading dislocation shape ($y = y(x)$ on x–y plane).

fluctuations. Noting that the strain is a relative quantity, a small simulation cell yields very high strain rates although the real dislocation velocity is sufficiently low as compared to the shear-wave velocity. The observed bias of the plastic strain toward positive values results from the pinning and attractive effect of the SFTs, which drive the dislocation towards them. In order to characterize these signals, we calculate a pair correlation

$$C_{\mathrm{p}}(\Delta t, q) = \langle |\gamma(t)\gamma(t+\Delta t)|^q \rangle_t \tag{15a}$$

and a height difference correlation,

$$C_{\mathrm{h}}(\Delta t, q) = \langle |\gamma(t) - \gamma(t+\Delta t)|^q \rangle_t, \tag{15b}$$

where $\langle\,\rangle_t$ is the time-average.

The pair correlation C_{p} and the height difference correlation C_{h} are shown in Fig. 4(b) and (c), respectively. C_{p} at various orders of moments is constant for a wide range of the time difference Δt between the two data. Large fluctuation of C_{p} at larger Δt can be attributed to the insufficient number of data for averaging. The tendency of the constant C_{p} is reminiscent of the white-noise type thermal stresses $\langle \tau_{\mathrm{therm}}(t)\tau_{\mathrm{therm}}(t+\Delta t)\rangle \propto \delta(\Delta t)$, which is implemented in the SDD scheme. On the contrary, Fig. 4(c) indicates a power law of the height difference correlations over different time scales i.e. $C_{\mathrm{h}}(\Delta t, q) \propto t^{qH}$. Slopes of the curves H in the figure take values of about 0.8–0.85 as compared with $H = 1/2$ for ordinary Brownian motion. Since

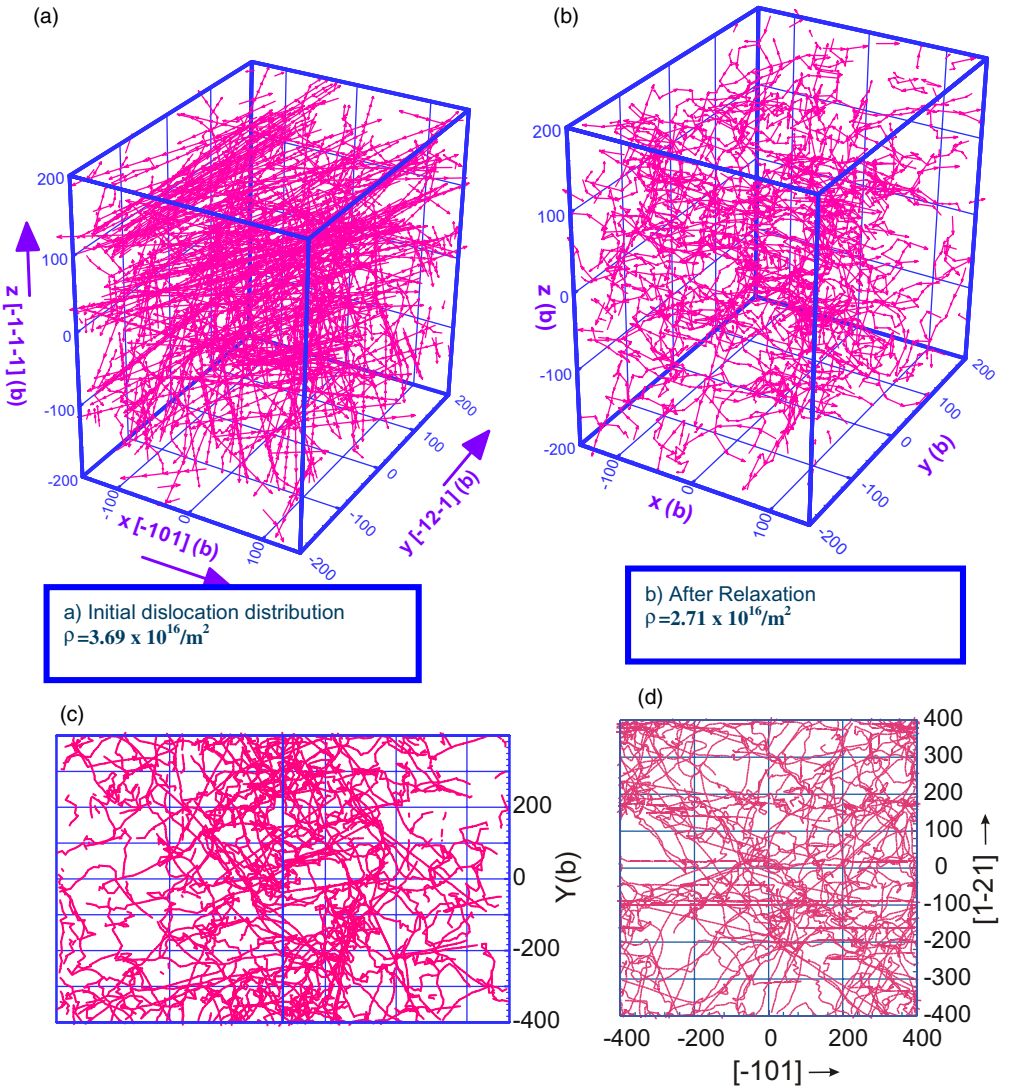

Fig. 5. (a) The initial random dislocation configurations of dislocations on (1 1 1) planes. (b) The dislocation structures 0.52 ns after relaxation viewed. (c) The dislocation structures 0.52 ns after relaxation viewed on (2 1 0) plane. (d) The dislocation structures 0.52 ns after relaxation viewed on (1 1 1) plane.

$C_h(\alpha\Delta t, q) = \alpha^{qH} C_h(\Delta t, q)$ for scale factor α, the data indicates the persistent of self-affine behavior of the fractional Brownian dislocation motion[34]. Deviation from the ordinary Brownian motion arises from the effect of the strain field of surrounding SFTs and self-avoiding nature of dislocations.

Using similar setting, results under creep conditions are obtained by the SDD simulations. The dislocations are subjected to a shear stress of 10 MPa. During loading, the dislocation density increases from $\sim 3.5\times10^{14}/m^2$ to $2.7\times10^{15}/m^2$. The result depicted in Fig. 4(d) shows a qualitatively different behavior of the height difference correlation from the previous case. Namely, the exponent H varies significantly according to the order of moment q. Within this specific range of q, H is a monotonically decreasing function of q with the values ranging from $\sim$0.25 to 1.2. Therefore, C_h shows a multifractal behavior with multiple exponents. Since it is persistent ($H > 1/2$) at lower q and anti-persistent ($H < 1/2$) at higher q, the system instability (larger fluctuation of time data of plastic strain) grows from higher order moments, while the deterministic nature stems from lower order moments. Considering the deduction obtained by Zaiser [23], this enhanced instability under load can be contribute to various spatial patterns for long run. Moreover, the self-affinity of the strain data obtained by the SDD simulations may emerge as macroscopic instability such as Portevin–Le Chatelier effect, which in fact shows similar SOC behavior [35].

Similar fractal analysis is performed for spatial patterns for the same dislocation-SFT binding configurations. Fig. 4(e) illustrates the height difference correlation for the shape of a threading dislocation on x–y plane: $C_h(\Delta x, q) = \langle |y(x) - y(x+\Delta x)|^q \rangle_x$, together with random dislocation orientation for references. Although it requires more complex functional forms for the scaling function for a wide range of distance along the dislocation (x), simple power relation holds for small Δx, implying again the SOC type fractal nature of the dislocation shape.

The formation of dislocation patterns using SDD simulations is further substantiated by the results shown in Fig. 5. These results pertain to the relaxation of dislocation curves that are distributed randomly in the 3D simulation cell. Fig. 5(a) shows the initial dislocation configuration, which consists mainly of straight dislocations with an initial density of $3.69\times10^{16}/m^2$. The SDD simulation is performed with no external applied loads. The dislocations are driven by their mutual interaction towards a meta-stable configuration shown in Fig. 5(b). Formation of dislocation cells can be deduced from the figure. This is also shown in the planar views given in Fig. 5(c) and (d). There are regions with very low dislocation density surrounded by regions with high dislocation density where the dislocation seems to be entangled. It should be pointed out here that cross-slip seems to play an important role in this case.

4. Summary and concluding remarks

In this paper, we investigated the problem of interaction of threading dislocations with immobile localized dislocation loops interaction. First, we examined the statistical properties of stable threading dislocation-loop configurations using Friedel–Kocks model. The obtained CRSS showed same functional forms as the original Friedel relation, with the deviation within several percent. On the other hand, the average dislocation segment length between the localized pinning loops indicated stress dependence stronger that that predicted by the Friedel relation. This difference can be explained based on the model assumptions: those obtained in this work are for static dislocation configurations in the athermal system while the Friedel relation is intended for meta-stable dislocation configurations in the steady motion. Second, we computationally explored the stochastic dislocation behavior leading to patterning using a recently developed stochastic dislocation dynamics code. Time signals of plastic strain showed scaling behaviors reminiscent of the self-organized criticality in their height-difference correlations. The moment dependence of the correlations was enlarged under load, corresponding to more deterministic and indeterministic dislocation behaviors in lower and higher order moments, respectively.

One can deduce form this and other studies that the discrete dislocation dynamics models are efficient when dealing with deformation at relatively small scales, say in the order of tens of micrometers. However, for deformation at larger spatial scales the use of continuum models becomes more efficient and inevitable. Nonetheless, even when developing such continuum models the DD analysis may provide a direct means for measuring corresponding internal variables (scalar and tensorial quantities). For instant, dislocations (threading dislocations and loops) in continuum crystal plasticity formulation can be modeled using non-Riemannian representation in terms of two second order rank tensors [36]: the torsion tensor α_{ij} (also called the Nye tensor) and the curvature tensor η_{ij}. These measures of geometric distortions can be directly computed from the plastic deformation stretch tensor γ of the continuum such that $\alpha_{ij} = -\varepsilon_{ikl}\gamma_{jk,l}$ and $\eta_{ij} = -(\varepsilon_{ikl}\alpha_{jk,l} + \varepsilon_{jkl}\alpha_{jk,l})/2$. In fact these two higher order gradients of the deformation field are the dislocation density tensor and dislocation flux tensor, respectively [37]. Thus, in the discrete system they can be computed explicitly for a given dislocation distribution [28], i.e. for a computational cell of volume V, containing a number of dislocation segments each with a Burgers vector $\boldsymbol{b}$, the Nye

tensor (or the dislocation density tensor) is given by $\alpha = \sum \frac{l_i}{V} b_i \otimes \xi_i$. While in the discrete system one can compute this tensor at every time step, in the continuum framework one needs to treat them as internal variables and establish evolution laws for them. For example, in order to model the evolution of dislocation structures, Shizawa and Zbib [38,39] proposed a set of coupled reaction–diffusion equations for α_{ij} and η_{ij} which under certain conditions lead to the formation of cell patterns. (In passing we note that for small strain, a set of these equations is known to form the Maxwell–Lorentz equations, showing analogue to an electromagnetic field to dislocation strain field.) The influence of these variables on deformation is directly incorporated in the hardening rules[40] providing an intrinsic length scale.

Recalling the geometric result $\operatorname{div}\alpha = 0$ [37] which is interpreted as continuity of dislocation, dislocation structures can always be decomposed into non-loop threading dislocations and Volterra dislocation loops, i.e. Burgers vectors on each dislocation line remains constant. This can be shown by applying Kirchoff theorem for the dislocation-network using analogue to electromagnetism. Representation by Somigliana dislocations where Burgers vectors varies along lines is redundant. In fact, Somigliana dislocations do not exist as isolated line defects because of the continuity of dislocations, although they are useful conceptually to consider problems of planer or membrane defects, twinnings, dislocations in polymers, or cracks. Therefore, it can be concluded that the first and the second order gradients of γ, α and η are the continuum representation of threading dislocations and Volterra loops, respectively.

Next we comment on the issue of the representative volume element (RVE) that a continuum model must be based upon. The question here is what is the 'appropriate' RVE over which the state of the material can be homogenized and macroscopic properties can be properly defined. But even after homogenization, the geometry of the RVE would depend on both the density of the threading dislocations that are referred to as geometrically necessary dislocations (GNDs) [41] and the density of the Volterra loops that are referred to as statistically stored dislocations (SSDs) since each group of these dislocations and the manner in which they are distributed in the cell contributes differently (on average over the RVE) to the changes in the material geometry. Thus, homogenous (local) quantities may not be sufficient to adequately capture the material response. In such cases, non-local quantities for $\bar{\gamma}(= (1/V_{\mathrm{RVE}}) \int_{V_{\mathrm{RVE}}} \gamma \, \mathrm{d}V)$, $\bar{\alpha}$ and $\bar{\eta}$ should be used to better denote plastic strains, GNDs, and SSDs, respectively, at the RVE level, leading to the use of higher order gradients.

For instant, in cases that the RVE contains many Volterra loops (or dipoles in a two dimensional model), the resulting eigenstrain should be represented by multipole expansions, which accompanies even higher order gradients of the plastic strain. Any combination of dislocation loops always forms multipoles with even order such as dipoles, quadrupoles, octapoles, etc., and, hence the superposition of $\nabla^2\bar{\gamma}$ (or akin terms such as $\nabla\bar{\gamma}\nabla\bar{\gamma}$), $\nabla^4\bar{\gamma}$, $\nabla^8\bar{\gamma}$, etc. can be used to specify the state of the internal strain in the RVE. Moreover, a complete list of reactions among these constituent dislocations and loops has to be obtained in order to correctly predict the dynamical evolution of the structure. Tabulation of all possible reactions is, however, a difficult task due to an unmanageably large number of these reactions when large RVEs are selected.

Only when relatively small RVEs are selected, local quantities may be replaced for non-local quantities without introducing higher order gradient terms, and the number of reactions between threading dislocations and loops can be manageably small in some cases. Considering the size of the dislocation core or minimum observable loops, such RVEs should be several nanometers at most. In other cases, the simple representation with lower order gradients of $\bar{\gamma}$ breaks down due to difficulties pertinent to physical situations, such as jogs formed by loop absorptions, or dilatation centers within the RVE. Fig. 6(a) and (b) illustrate multiple Volterra loops extracted from a jog and a dilation center that require higher order gradients.

Finally we note that the DD method is an important component in the multiscale modeling framework in which the material behavior can be obtained according to the spatial and/or time resolutions of interest, relating atomistic properties to macroscopic ones and eventually extracting *universal relations*. This approach has been successful in many non-dissipative closed systems [42]. As can be deduced from the previous section, the self-affinity of the height difference correlation $C_{\mathrm{h}}(\Delta t, q) \propto t^{qH}$ holds over a wide range of time scales, and similar scale invariant behavior has been obtained

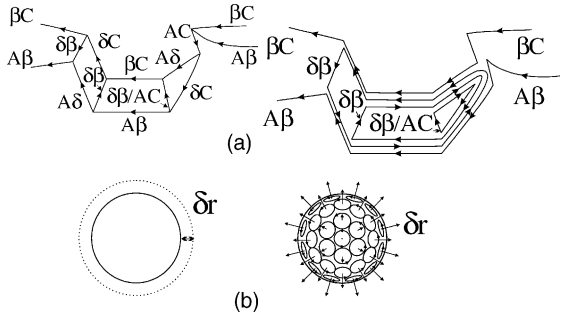

Fig. 6. (a) Decomposition of the jog formation (left) into a threading dislocation and Volterra loops (right). The initial extended jog formation is obtained by a MD simulation [32]. (b) Decomposition of the dilatation center with change in the effective radius δr (left) into Volterra loops with Burgers vector δr (right).

in macroscopic experiments. Such relation implies that the simulated dislocation system is near the critical states. If we conjecture a more general scaling relation for both temporal and spatial quantities such as $f(\alpha r, p; \beta t, q) \propto \alpha^{pJ(p)}\beta^{qK(q)} f(r, p; t, q)$, the fractal behavior obtained in macroscopic experiments can be extrapolated into smaller time scales as well as shorter spatial scale, providing guidance to generic constitutive laws in continuum plasticity. Obviously, comprehensive study spanning microscopic to macroscopic plasticity is needed to confirm the scaling hypothesis.

Acknowledgements

The support of the DOE (grant DE-FG03-01ER54629) and the Lawrence Livermore National Laboratory (contract W-7405-Eng-48) is gratefully acknowledged. Special thanks to Mr Shafique Khan for his valuable comments.

Appendix A

The eigensystem of the cyclic matrix T in Eq. (5a) is determined below. We define E_j as the $n \times n$ unit matrix, and S as the $NM \times NM$ cyclic matrix, $S = \begin{pmatrix} 0 & 1 \\ E_{NM-1} & 0 \end{pmatrix}$.

According to such transitional cyclic character of the matrix S that

$$S^2 = \begin{pmatrix} 0 & E_2 \\ E_{NM-2} & 0 \end{pmatrix}, \quad S^3 = \begin{pmatrix} 0 & E_3 \\ E_{NM-3} & 0 \end{pmatrix}, \ldots, S^{NM-1} = \begin{pmatrix} 0 & E_{NM-1} \\ E_1 & 0 \end{pmatrix} \tag{A.1}$$

one finds the matrix T in the form of a polynomial of S as

$$T = f(S) = \sum_{m=0}^{M-1} p_m S^m. \tag{A.2}$$

The secular equation for S is $\lambda^{NM} - 1 = 0$ and the eigenvalue λ is obtained as

$$\lambda = \varsigma^n, \tag{A.3}$$

where $\varsigma = \exp(2\pi \mathrm{i}/MN)$ and $(0 \leqslant n \leqslant NM - 1)$.

The corresponding eigenvectors are

$$V_n = \left(\varsigma^{n(NM-1)}\varsigma^{(n-1)(NM-1)} \cdots \varsigma^{2n}\varsigma^{n} 1\right)^t. \tag{A.4}$$

Then the unitary matrix of T is given as

$$U = (NM)^{-1/2}(V_0 V_1 \cdots V_{NM-1}). \tag{A.5}$$

Since S and T are commutable, T can be diagonalized by the unitary matrix U of S. Defining the diagonal matrix as

$$D = U^+ S U = \mathrm{diag}\left\{1, \varsigma, \varsigma^2, \ldots, \varsigma^{NM-1}\right\} \tag{A.6}$$

similarly, T can be diagonalized as

$$U^+ T U = U^+ f(S) U = \sum_{m=0}^{M-1} p_m D^m = \mathrm{diag}\left\{f(1), f(\varsigma), f(\varsigma^2), \ldots, f(\varsigma^{NM-1})\right\}. \tag{A.7}$$

Finally, a matrix element of T^N can be obtained as

$$T^N_{q+1,1} = \left[U(U^+ T U)^N U^+\right]_{q+1,1} = (NM)^{-1} \sum_{n=0}^{NM-1} f(\varsigma^n)^N \varsigma^{-nq}. \tag{A.8}$$

References

[1] J. Friedel, Dislocations, Addison-Wesley, Reading, Mass, 1967.
[2] K. Hanson, J.W. Morris Jr., J. Appl. Phys. 46 (3) (1975) 983.
[3] K. Hanson, J.W. Morris Jr., J. Appl. Phys. 46 (6) (1975) 2378.
[4] R.e.a Labusch, Phys. Stat. Sol. 41 (1970) 659.
[5] R. Labush, J. Appl. Phys. 48 (1977) 4550.
[6] B. Reppich et al., Mater. Sci. Eng. 83 (1986) 45.
[7] E. Nadgorny, in: J.W. Christian, P. Haasen, T.B. Massalski (Eds.), Progress in Materials Science, vol. 31, Pergamon, Oxford, 1988, p. 530.
[8] M. Hiratani, PhD thesis, MTU, 2000.
[9] M. Hiratani, H.M. Zbib, J. Eng. Mater. Technol. 124 (2002) 335.
[10] T.J. Koppenaal, D. Kuhlmann-Wilsdorf, Appl. Phys. Lett. 4 (1964) 59.
[11] U.F. Kocks, in: P. Haasen, V. Gerold, G. Kostorz (Eds.), ICSMA 5, vol. 1, Pergamon, Oxford, 1980, p. 1661.
[12] L.M. Brown, R.K. Ham, in: A.A.N. Kelly, R.B. Nicholson (Eds.), Strengthening Methods in Crystals, Applied Science, London, 1971.
[13] H.M. Zbib, M. Rhee, J.P. Hirth, in: T. Abe, T. Tsuta (Eds.), Advances in Engineering Plasticity and its Applications, Pergamon, NY, 1996, p. 15.
[14] H.M. Zbib, M. Rhee, J.P. Hirth, Int. J. Mech. Sci. 40 (1998) 113.
[15] M. Rhee et al., Model. Simulat. Mater. Sci. Eng. 6 (1998) 467.
[16] H.M. Zbib et al., J. Nucl. Mater. 276 (2000) 154.
[17] M. Kiritani, J. Nucl. Mater. 276 (2000) 41.
[18] B.V. Petukhov, Mater. Sci. Eng. A 234–236 (1997) 177.
[19] J. Gil Sevillano, E. Bouchaud, L. Kubin, Scr. Metall. Mater. 25 (2) (1991) 355.
[20] S.I. Zaitsev, Physica A 189 (1992) 411.
[21] R. Thomson, L.E. Levine, Phys. Rev. Lett. 81 (1998) 3884.
[22] D.A. Hughes et al., Phys. Rev. Lett. 81 (1998) 4664.

[23] M. Zaiser, Mater. Sci. Eng. A 309&310 (2001) 304.
[24] D.C. Chrzan, M.S. Daw, Phys. Rev. B 55 (2) (1997) 798.
[25] L.P. Kubin, Phys. Stat. Sol. (a) 135 (1993) 433.
[26] N.M. Ghoniem, L. Sun, Phys. Rev. B 60 (1999) 128.
[27] K. Schwartz, Phys. Rev. 79 (1997) 1877.
[28] H.M. Zbib, T. Diaz de la Rubia, Int. J. Plasticity 18 (9) (2002) 1133.
[29] D. Raabe, Comput. Mater. Sci. 11 (1998) 1.
[30] D. Ronnpagel, T. Streit, T. Pretorius, Phys. Stat. Sol. 135 (1993) 445.
[31] M. Hiratani, H.M. Zbib, M.A. Khaleel, Int. J. Plasticity 19 (2003) 1271.
[32] T. Rasmussen, K.W. Jacobs, Phys. Rev. B 56 (6) (1997) 2977.
[33] S. Rao, T.A. Parthasarathy, C. Woodward, Philos. Mag. A 79 (1999) 1167.
[34] J. Feder, Fractals, Prenum, New York, 1988.
[35] G. Annthakrishna et al., Mater. Sci. Eng. A 309&310 (2001) 316.
[36] T. Hasebe, Y. Imaida, Acta Metall. Sin. 11 (6) (1998) 405.
[37] T. Mura, Micromechanics of Defects in Solids, Kluwer, Netherlands, 1982.
[38] K. Shizawa, K. Kikuchi, H.M. Zbib, Mater. Sci. Eng. A 309&310 (2001) 416.
[39] K. Shizawa, H.M. Zbib, in: A. Khan (Ed.), Proceedings of the 7th International Symposium on Plasticity and its Current Applications, Neat, 1999, p. 519.
[40] T. Ohasihi, Philos. Mag. Lett. 75 (2) (1994) 51.
[41] M.F. Ashby, in: A.K.a.R.B. Nicholson (Ed.), Strengthening Methods in Crystals, Elsevier, Amsterdam, 1971, p. 184.
[42] K.G. Wilson, Rev. Mod. Phys. 47 (1975) 773.